



CHORUS

This is the accepted manuscript made available via CHORUS. The article has been published as:

Optical decoherence and energy level structure of $0.1\%Tm^{3+}:LiNbO_3$

Y. Sun, C. W. Thiel, and R. L. Cone

Phys. Rev. B **85**, 165106 — Published 6 April 2012

DOI: [10.1103/PhysRevB.85.165106](https://doi.org/10.1103/PhysRevB.85.165106)

Optical Decoherence and Energy Level Structure of 0.1%Tm³⁺:LiNbO₃

Y. Sun*

*Department of Physics, The University of South Dakota, Vermillion, South Dakota 57069
and Department of Physics, Montana State University, Bozeman, Montana 59717*

C. W. Thiel[†] and R. L. Cone[‡]

Department of Physics, Montana State University, Bozeman, Montana 59717

(Dated: March 26, 2012)

We report the energy level structure of the ³H₆ and ³H₄ multiplets for Tm³⁺ doped congruent LiNbO₃, as well as the decoherence properties and their temperature dependencies for the ³H₆(1) ↔ ³H₄(1a) transition at 794 nm. It is shown that this material provides very significant improvements in bandwidth, time-bandwidth product, and sensitivity for spatial-spectral holographic signal processing devices and quantum memories based on spectral hole burning. The available signal processing bandwidth for 0.1% Tm³⁺:LiNbO₃ is 300 GHz versus 20 GHz for Tm³⁺:YAG. The peak absorption coefficient for 0.1% Tm³⁺:LiNbO₃ is 15 cm⁻¹ at 794.5 nm compared with 1.7 cm⁻¹ for 0.1% Tm:YAG at 793 nm, and the total absorption strength is eighty times stronger. The oscillator strength for Tm³⁺:LiNbO₃ is about twenty five times larger than that for Tm³⁺:YAG, making the material five times more sensitive for processing high-bandwidth analog signals. The homogeneous linewidth, which determines processing time or spectrum analyzer resolution, is 30 kHz at 1.6 K and 350 kHz at 6 K, as measured by photon echoes. Those values establish potential time-bandwidth products of 10⁷ and 7 × 10⁵ respectively. The temperature dependence of the homogeneous linewidth was explained by observation of a 7.8 cm⁻¹ crystal field level in the ground multiplet and direct phonon coupling. The excited state ³H₄ lifetime T₁ is 152 μs and the bottleneck lifetime of the lowest ³F₄ level is 7 ms from photon echo measurements. These factors combine to provide a surprisingly large increase in key parameters that determine material performance for spatial-spectral holography, quantum information, and other spectral hole burning applications.

PACS numbers: 76.30.Kg, 42.70.-a, 42.50.Md, 78.47.jh, 42.62.Fi

I. INTRODUCTION

Trivalent thulium doped crystals have been used in spatial-spectral holography applications (SSH)¹ and Quantum Information Science. Applications include high bandwidth analog signal processing such as spectrum analysis, radar and lidar processing, signal digitization,^{2,3} generation of true-time delays⁴ and arbitrary optical waveforms, and quantum memories to serve as repeaters for secure quantum communication.⁵⁻¹⁰ Entanglement storage of photons has been demonstrated in Tm³⁺:LiNbO₃ in Ref. 10. The success of those demonstrations illustrates the importance of finding, characterizing, and developing Tm³⁺ materials capable of superior or complementary properties. For Tm³⁺:YAG, the material that has been used for many of these applications, the main drawbacks have been that the oscillator strength is relatively small and the ~20 GHz processing bandwidth, which is determined by the inhomogeneous linewidth, is relatively narrow for some applications. As we show in this paper, Tm³⁺:LiNbO₃ allows one to expand device bandwidth into the microwave and millimeter wave regions where many of the SSH devices cited above can exceed the performance of state-of-the-art electronics.

Here we report the energy level structure of the ³H₆ and ³H₄ multiplets for Tm³⁺ doped congruent LiNbO₃ obtained by absorption, site-selective fluorescence spectroscopy, as well as the coherence properties and their temperature dependencies for the ³H₆(1) ↔ ³H₄(1a) tran-

sition. The lineshapes and degeneracies were characterized and modeled. The portion of the energy level structure used in the coherence measurement is described in Fig. 1. The two lowest ³H₆ levels were found to be 7.8 cm⁻¹ apart and were all of singlet character and the lowest ³H₄ levels were found to be a split doublet due to distortions from the expected C₃ symmetry. We label the doublet as ³H₄(1) in general and when clearly identified, as ³H₄(1a) for the lower component and ³H₄(1b) for the upper component of the doublet. The gap between the split levels was found to range from 7.3 cm⁻¹ to 15 cm⁻¹ and the line shape can be attributed to overlapping transitions for five main sites. The Zeeman effect of a spectral hole burned in the line shape further confirms that the doublet is split for this material. The spontaneous emission lifetime of the ³H₄(1a) level was measured by three-pulse photon-echo decay and by the decay of a spectral hole. It is very close to the expected lifetime from the measured oscillator strength.

Two-pulse photon echo measurements of decoherence are described along with the excitation profile for photon echoes. That analysis is followed by spectral diffusion measurements to evaluate the mechanisms responsible for the observed non-exponential decoherence. The 7.8 cm⁻¹ energy level in the ³H₆ multiplet explained the temperature dependence observed in the decoherence measurements.

Decoherence measurements for the relevant levels not only served to characterize the material properties criti-

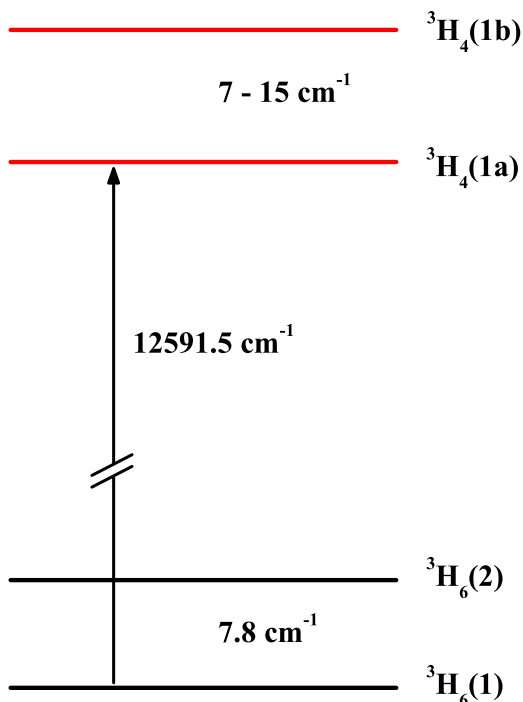


FIG. 1: Relevant portion of $\text{Tm}^{3+}:\text{LiNbO}_3$ energy level structure and labels derived from the absorption and emission experiments.

cal for spatial-spectral holography and quantum information applications, they also provided further confirmation of the basic level structure and lineshape analysis. In combination, these measurements provided insight into the multiple Tm^{3+} sites and disorder of the congruent LiNbO_3 .

These studies demonstrate that even with a dramatically broadened inhomogeneous line as a consequence of significant crystal disorder, the homogeneous linewidth can still be narrow enough to give very large time-bandwidth product as the ratio of inhomogeneous to homogeneous line widths. That, together with the exceptionally large transition probabilities, provides the desired parameters for significant improvements in performance compared to $\text{Tm}^{3+}:\text{YAG}$.

II. EXPERIMENTAL DETAILS

The crystal structure of LiNbO_3 has been reported by Weis and Gaylord.¹¹ There are numerous studies of rare earth dopant ions substitutionally occupying multiple perturbed sites in doped LiNbO_3 ; for example, Dierolf¹² reviews optical studies of Er^{3+} , which has a very similar ionic radius to that of Tm^{3+} . Rare earth dopant sites for a variety of ions also have been presented by Malovichko et al.¹³ who have studied the structure with ENDOR. In LiNbO_3 , the Tm^{3+} ions occupy multiple charge compensated sites, and general disorder has been reported.^{14–18}

TABLE I: Electric dipole selection rules for C_3 point symmetry. Consistent with conventional definitions, π denotes linear polarization with $E\parallel c$ and σ denotes linear polarization with $E\perp c$; α denotes circular polarization with light propagating along c .

	A	E
A	π	σ, α
E	σ, α	π, σ, α

Typically, rare earth ions substitute for Li^+ ions. Rutherford backscattering experiments by Lorenzo et al.¹⁹ reported no occupancy of Nb^{3+} sites, and our spectroscopy, polarization selection rule properties, and lineshape simulations all appear to be consistent with occupation of only Li^+ sites. In our experiments, as we shall see, the spectra manifested the basic polarization properties characteristic of the C_3 local symmetry of Li^+ sites. A modest distribution of crystal field splittings, modified by lattice perturbations such as non-local charge compensations, gives rise to very broad lines. We attribute the broad linewidths to a superposition of inhomogeneous broadening and overlapping transitions from the multiple sites. In the measurements reported below, five or more similar charge-compensated sites appear to contribute to the lineshapes.

The experiments were all carried out in an Oxford Optistat liquid helium bath cryostat with active temperature control. For absorption experiments, a halogen lamp and a SPEX 14018 double monochromator were used. For emission and photon echo experiments, a Coherent 899-21 single-frequency Ti:Sapphire laser was used, and the required pulses were gated by two 80 MHz acousto-optic modulators in series.

Several samples of nominally 0.1% $\text{Tm}^{3+}:\text{LiNbO}_3$ with congruent composition were prepared by Scientific Materials Corporation of Bozeman, MT. Crystals were grown by the rf-heated Czochralski method. These crystals were oriented and cut with surfaces perpendicular to the c -axis and the a axes. Samples of various thicknesses were used for elucidating different regions of the parameter space due to large differences in the absorption coefficients for different transitions.

III. ABSORPTION EXPERIMENTS AND THE ${}^3\text{H}_4$ LEVEL STRUCTURE

For C_3 symmetry, three singlet A levels and three doublet E levels are expected for the ${}^3\text{H}_4$ state and five A and four E levels for the ${}^3\text{H}_6$ state. The ${}^3\text{H}_6 \rightarrow {}^3\text{H}_4$ transitions are expected to be primarily electric dipole since $\Delta J > 1$. The electric-dipole selection rules for C_3 symmetry are listed in Table I. Absorption spectra with π and σ polarizations with light propagating along the crystal a -axis were recorded and are shown in Fig. 2.

The lowest energy ${}^3\text{H}_6(1) \rightarrow {}^3\text{H}_4(1)$ transition has by

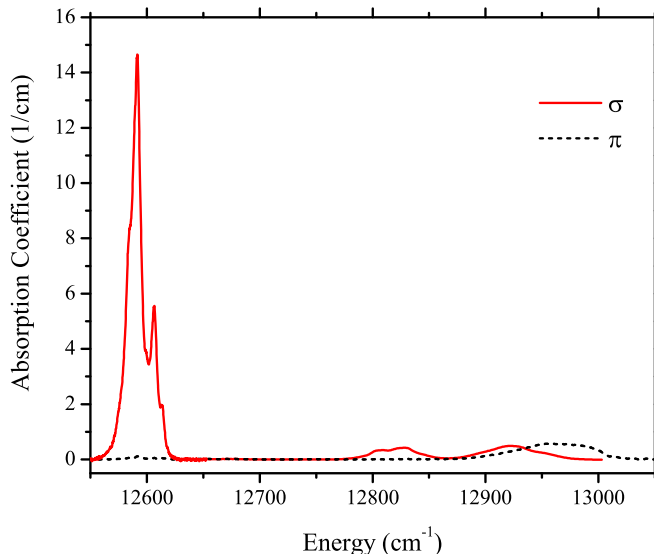


FIG. 2: Polarized absorption coefficients for 0.1%Tm³⁺:LiNbO₃ at 1.6 K, showing the ³H₄ level structure. The strongest low energy peak on the left is the ³H₆(1)→³H₄(1) transition of interest for spatial-spectral holography and other coherence applications, including quantum information. The spectra are strongly polarized. The strong (1)→(1) transition is σ polarized with $E \perp c$.

far the strongest absorption in the entire spectrum and is also the transition of primary interest for SSH, quantum information, and other applications requiring long coherence and narrow spectral holes. That transition is much stronger than the corresponding ³H₆(1)→³H₄(1) transition for Tm³⁺:YAG. Since the σ polarized ³H₆(1)→³H₄(1) transition was so strong, it was measured using a 0.91 mm thick sample, while the weaker π polarized spectrum and other σ polarized transitions were measured with a thicker 9 mm sample.

Usually, absorption linewidths for transitions to the upper levels of a J-multiplet are dominated by non-radiative decays of the upper level and have Lorentzian profiles with monotonically increasing linewidths. In this case, however, transitions to all levels of the ³H₄ multiplet have lineshapes spanning 30 to 50 cm⁻¹, values that are unusually large. The lineshapes and linewidths of the transitions, described in detail below, are attributed to a distribution of energy level shifts arising from a distribution of perturbed sites with varied crystal-field and free-ion interactions.

For the ³H₄ multiplet, there should be three singlets and three doublets, for a total of six energy levels. Only three σ transitions and one π transition were apparent for the spectra in Fig. 2. Around 12 665 to 12 747 cm⁻¹, however, two weaker π transitions were readily observed on an expanded vertical scale. Those two transitions showed a degree of mixed polarization, perhaps indicating that they are intrinsically very weak and are gaining additional intensity as a result of perturbation from the

TABLE II: Observed ³H₄ energies from ³H₆(1)→³H₄ absorption transitions. All absorption linewidths were around 30 cm⁻¹, indicating a distribution of crystal fields for a distribution of moderately perturbed sites. Since all transitions had similar linewidths, peak absorption coefficients are listed to indicate transition intensities.

E (cm ⁻¹)	Abs. Coeff.	³ H ₄ Irrep.	Polar.	E (cm ⁻¹) (Ref. 20)
12591.5	14.6	E	σ	12602.3
12665	<0.015	A	π	12655.7
12747	<0.015	A	π	12739.5
12821.3	0.39	E	σ	12825.0
12923.5	0.48	E	σ	12928.8
12958.0	0.61	A	π	12969.8

nominal C₃ symmetry.

From the polarization dependence, there was very little mixing of polarizations for any of the four stronger transitions, so we concluded that the C₃ irreducible representations remain useful state labels and that the assignment for the ground state is A or Γ_1 , consistent with the assignment in Ref. 20. If the ground state was an E state or $\Gamma_{2,3}$, transitions for both polarizations would have been expected. The observed ³H₄ energies and assigned C₃ representations are listed in Table II. The irreducible representations listed there for all levels are identical to those in Ref. 20, but our more accurately determined energy values are significantly different from theirs.

With the large inhomogeneous broadening observed for all the ³H₆(1)→³H₄ absorption lines, one cannot simply specify the ³H₄ energy levels in the traditional manner with a single number. In Table II the center of the largest peak at 12591.5 cm⁻¹ is listed as the energy of the ³H₆(1)→³H₄(1) transition (The centroid of this transition is at 12592.3 cm⁻¹). The centroids of the absorption lines are listed for all other levels in the multiplet. The line positions and absorption coefficients of the two weak transitions at 12665 and 12747 cm⁻¹ were less certain, but the polarization dependence allowed us to assign symmetry labels. The overall spread in the transition energies appears to be similar for all transitions including the higher transitions, indicating the presence of both homogeneous and inhomogeneous broadening in the lineshapes, including those of upper levels of the multiplets.

The primary transition having long decoherence times is usually the transition from the lowest component of the ground multiplet to the lowest component of the excited multiplet. Considerable structure is evident in the lineshape of the ³H₆(1)→³H₄(1) transition due to the multiple rare earth sites present in the crystal. It was also found that the structure is quite sensitive to temperature. To elucidate the structure and the temperature dependence of this transition, absorption spectra at 1.6 K, 11 K, 20 K, and 41 K were taken and analyzed. A low-lying ³H₆(2) level, at 7.8 cm⁻¹ above the ground

state, is found from this analysis and absorption from this level, which can be populated at elevated temperatures, contributes significantly to the absorption lineshape.

In Fig. 3, we present the absorption spectra at 1.6 K and 11 K. It is obvious that spectra at those two temperatures are quite different. In the 1.6 K spectrum, the absorption is due to the transition from the ${}^3\text{H}_6(1)$ ground state only and we label the two strongest peaks as A and B (not to be confused with the site's symmetry group notation). In the 11 K spectrum, a peak labeled C appears at 7.8 cm^{-1} below the A peak and the peaks A and B become weaker compared to the 1.6 K spectrum. We attribute the appearance of the C peak to the transition from the thermally populated ${}^3\text{H}_6(2)$ level and the weakening of peaks A and B to the reduced population in the ground state. We suggest that peaks A and C correspond to absorptions to the same upper level from ${}^3\text{H}_6(1)$ and ${}^3\text{H}_6(2)$, respectively. Based on this assumption, at 11 K, 27% of the population should be in the ${}^3\text{H}_6(2)$ state while 73% should be in the ground state according to the Boltzmann distribution, reducing the absorption from the ground state to 73% of its strength at 1.6 K. To isolate the absorption spectrum from ${}^3\text{H}_6(2)$, we scaled the 1.6 K data by a factor of 73% and subtracted it from the 11 K spectrum, as shown by the dashed line in Fig. 3. The inferred lineshape (dashed) is similar to but not identical to that of the ${}^3\text{H}_6(1)\text{-}{}^3\text{H}_4(1)$ transition taken at 1.6 K, but such differences are expected since the energy of the ${}^3\text{H}_6(2)$ level can vary for each of the multiple sites that contribute to the overall line broadening, and the 7.8 cm^{-1} value for this energy is an average, although the variation of the energy gap is small. We label the two main peaks in the inferred spectrum A' and B'. Comparing the inferred spectrum and the 1.6 K spectrum, we find that the energy difference between peaks labeled A and A' and that between B and B' are each 7.8 cm^{-1} , further confirming the assignment of the C peak. Thus, we conclude that the second component of the ground ${}^3\text{H}_6$ multiplet is located at 7.8 cm^{-1} . This determination was further confirmed by the low temperature emission spectra reported in Section V.

The total absorption strength for any transition, defined as the integral of the absorption coefficient with energy, has an experimentally convenient unit that is the product of the absorption coefficient in cm^{-1} and the linewidth in cm^{-1} . The absorption strength for the ${}^3\text{H}_6(1)\text{-}{}^3\text{H}_4(1)$ transition is 250 cm^{-2} at 1.6 K. The total absorption strength under the dashed line, which corresponds to the absorption for the ${}^3\text{H}_6(2)\text{-}{}^3\text{H}_4(1)$ transition with 27% of the population at 11 K, is 90 cm^{-2} . The oscillator strength of the ${}^3\text{H}_6(2)\text{-}{}^3\text{H}_4(1)$ transition may be estimated by considering the transition strength of the ${}^3\text{H}_6(1,2)\text{-}{}^3\text{H}_4(1)$ absorptions at different temperatures and the corresponding populations of the ${}^3\text{H}_6(1)$ and ${}^3\text{H}_6(2)$ levels determined by the Boltzmann distribution. From analysis of the absorption spectra at 1.6 K, 11 K, 20 K, and 41 K, we concluded that the ${}^3\text{H}_6(2)\text{-}{}^3\text{H}_4(1)$ transition is 1.35 ± 0.1 times as strong as the

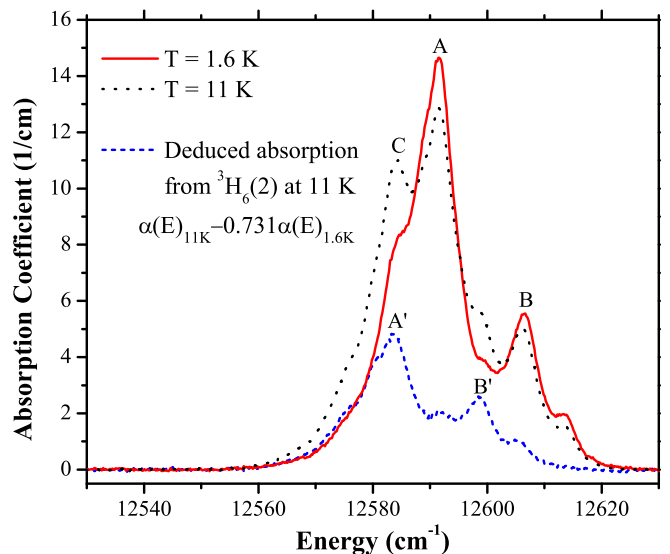


FIG. 3: (Color online) Absorption coefficients for σ polarization in $0.1\% \text{ Tm}^{3+}:\text{LiNbO}_3$ at 1.6 K and 11 K in the vicinity of the ${}^3\text{H}_6(1)\text{-}{}^3\text{H}_4(1)$ transition showing inhomogeneous broadening and transitions from the ${}^3\text{H}_6(2)$ level. The absorption from the thermally populated ${}^3\text{H}_6(2)$ level at 11 K (dashed line) was isolated from that from ${}^3\text{H}_6(1)$ by a subtraction process described in the text.

${}^3\text{H}_6(1)\text{-}{}^3\text{H}_4(1)$ transition.

The B and B' peaks and the weak peaks above them in energy are attributed to the splitting of the ${}^3\text{H}_4(1)$ doublet by perturbations from perfect C_3 symmetry due to moderately distant charge compensation. The upper component of this doublet is labeled ${}^3\text{H}_4(1b)$ and the lower component ${}^3\text{H}_4(1a)$ in subsequent discussions. Since the C_3 symmetry can be broken in different ways depending on the various manners that charge compensation can be achieved, we do not expect these splittings to be the same for each perturbed site. Echo excitation results confirm that the upper ${}^3\text{H}_4(1b)$ levels give no readily observable echo and thus have very short decoherence times.

For polarized spectra, the relationship^{21,22} between the absorption strength and the oscillator strength can be generalized to

$$f_{12} = \frac{m_e c^2}{\pi e^2} \frac{1}{N} \frac{1}{3} \sum_i \frac{9n_i}{(n_i^2 + 2)^2} \int \alpha_i d\sigma \quad (1)$$

where N is the ion number density, n_i is the index of refraction for polarization in the i (x , y , or z) direction, α_i is the absorption coefficient, and σ is the transition energy in wavenumbers. To calculate the oscillator strength of the ${}^3\text{H}_6(1)\text{-}{}^3\text{H}_4(1)$ transition, we use the ion number density of $1.89 \times 10^{19}\text{ cm}^{-3}$ (corresponding to 0.1 atomic %), index of refraction of 2.256, and $\sum \int \alpha_i d\sigma = 497\text{ cm}^{-2}$ for the a and a' directions. The local field correction $9n/(n^2 + 2)^2$ is 0.404. The calculated oscillator strength is thus found to be 4.0×10^{-6} for the transition from the

ground state singlet to both components of the excited state doublet. Since the excited state doublet is split due to deviation from C_3 symmetry, the useful oscillator strength of $Tm^{3+}:LiNbO_3$, i.e., for the transition from the ground state to the lower component of the excited state doublet, is thus 2.0×10^{-6} , 25 times larger than that of $Tm^{3+}:YAG$,²³ which has a value of 8×10^{-8} . This represents a very substantial performance increase for thulium materials, providing for higher speed and higher time-bandwidth product in applications.

IV. ZEEMAN EFFECT FOR A SPECTRAL HOLE

As discussed earlier, for ideal C_3 symmetry we expect the $^3H_4(1)$ excited state of Tm^{3+} to be a paramagnetic doublet. However, time-reversed orbital doublets like these E states are particularly sensitive to weak perturbations of the point symmetry. The required charge compensation of the trivalent ion could break the perfect crystal symmetry and cause the doublet to be split as we have seen in the absorption experiments. As a result, we explored this effect by examining the Zeeman shifts of the optical transition in an applied magnetic field to confirm the validity of the assignment.

While the traditional approach for observing the Zeeman splitting of the excited state is to directly monitor the splitting and shift of the optical absorption lines, this is not practical for $Tm:LiNbO_3$ due to the large inhomogeneous broadening and complex spectral structure. Consequently, we used a spectral hole burning technique to determine the Zeeman shift.²⁴

To probe the Zeeman effect directly, we burned a persistent spectral hole with an applied magnetic field and then changed the magnitude of the applied field and observed the resulting shift of the spectral hole. This is shown in Figure 4 for a change in applied field of 310 G with $B \parallel c$ -axis. We observe the expected splitting of the spectral hole due to the nuclear Zeeman effect shifting the hyperfine level splittings, with the value of 1.3 GHz/T in agreement with our earlier antihole shift measurements.²⁵

In addition to the expected effect from the ^{169}Tm nuclear levels, we also observe a shift in the center of gravity of the spectral hole structure to lower frequency with a shift of 1 GHz/T. This effect can only be described by a magnetic moment of the Tm^{3+} electronic states. Since we only observe a shift and not a splitting, this result demonstrates that the electronic degeneracy is in fact broken and that the E doublet is split. The relatively small Zeeman shift of 1 GHz/T arises from a second order Zeeman effect, consistent with the earlier assignment.

Also, spectral hole burning across the inhomogeneous line revealed different nuclear Zeeman splittings at different frequencies, as well as multiple splittings at some frequencies. This agrees with our analysis of the spectral line shape discussed in the next section, further confirm-

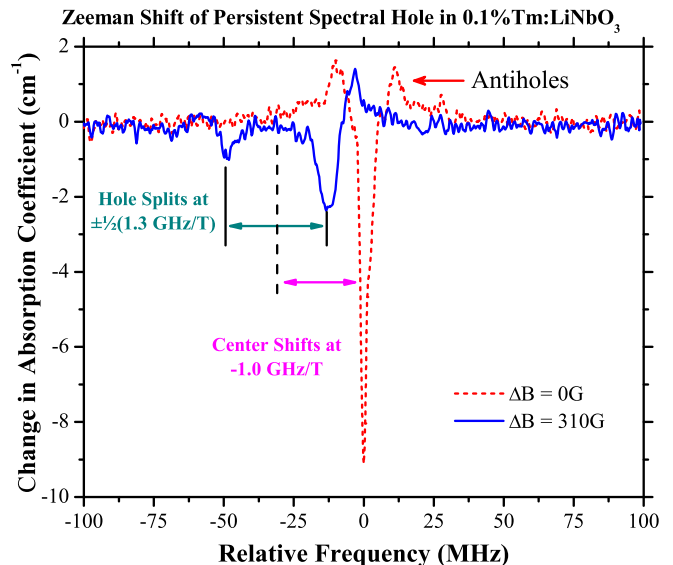


FIG. 4: Observation of magnetic splitting and shift of spectral holes revealing the weak Zeeman effect in the electronic excited state of $Tm^{3+}:LiNbO_3$.

ing our assignment of multiple sites contributing to the line shape.

V. EMISSION EXPERIMENTS AND THE 3H_6 LEVEL STRUCTURE

Emission experiments were carried out to determine the level structure of the 3H_6 multiplet and to confirm the assignment of the low-lying $^3H_6(2)$ level at 7.8 cm^{-1} . To avoid possible modifications of the spectrum due to spectral hole burning, the cw pumping laser was tuned to excite the fifth level in the 3H_4 multiplet. At 1.6 K, the $^3H_4(5)$ population is expected to relax by spontaneous phonon emission to the $^3H_4(1)$ level on a time scale much shorter than the fluorescence lifetime, so emission should come only from $^3H_4(1a)$. When different parts of the $^3H_4(5)$ absorption line were excited, emission lineshapes remained the same for transitions to $^3H_6(3)$ and higher levels of 3H_6 but they changed dramatically for transitions to $^3H_6(1)$ and (2), implying that the $^3H_6(1) \rightarrow ^3H_4(5)$ absorption is still inhomogeneously broadened. It also implies that the emission spectra should not be used for the determination of the energy of the $^3H_4(1)$ level.

The polarized emission spectra for laser excitation at 12920 cm^{-1} are presented in Fig. 5. Comparing the spectra of Fig. 5 with the absorption spectra in Fig. 2, the strongest transition is shifted to somewhat lower energy than the 12591.5 cm^{-1} of the A peak value from the σ -polarized absorption spectrum of Fig. 2. The strong group of emission lines centered around 12580 cm^{-1} is assigned to an overlapping combination of the $^3H_4(1a) \rightarrow ^3H_6(1)$ and (2) transitions for all of the sites.

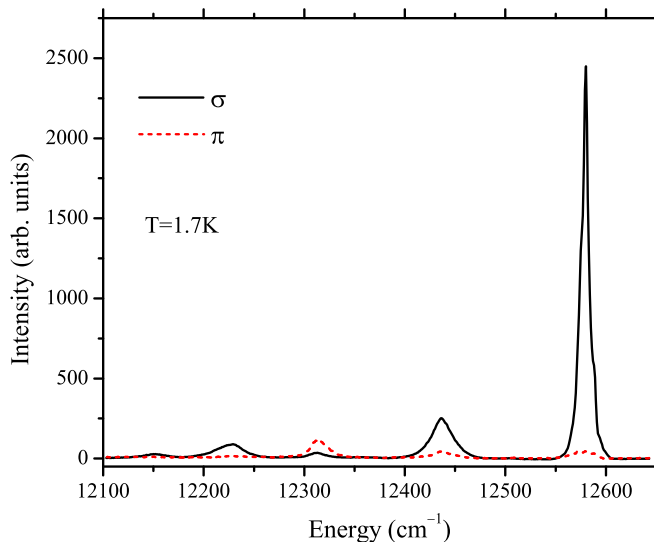


FIG. 5: Polarized emission spectra for 0.1% $\text{Tm}^{3+}:\text{LiNbO}_3$ at 1.6 K following cw laser excitation. The strongest σ polarized peak on the right is a combination of the ${}^3\text{H}_4(1a) \rightarrow {}^3\text{H}_6(1,2)$ transitions, which are shown in greater detail in Fig. 6.

It should be noted that the ${}^3\text{H}_4(1a) \rightarrow {}^3\text{H}_6(2)$ transition is not reduced by a Boltzmann factor as was the case for the absorption spectrum, but rather, it is 1.35 times stronger as stated in Sec. III. In the emission experiment, the Tm^{3+} sites are not excited uniformly as a consequence of the inhomogeneous broadening in the ${}^3\text{H}_4(5)$ level. No emission was seen at energies above 12600 cm^{-1} , consistent with our assertion that the B peak in the absorption spectra and peaks associated with it are due to the upper level of the split ${}^3\text{H}_4(1)$ doublet. In the emission spectrum, no emission from the ${}^3\text{H}_4(1b)$ level was observed.

Energy transfer among the multiple sites that were partially resolved in the ${}^3\text{H}_6(1)$ to ${}^3\text{H}_4(1)$ absorption spectrum was investigated by directly exciting the ${}^3\text{H}_4(1)$ level with a tunable laser. The site selective spectra, over a range of 70 cm^{-1} , are shown in Fig. 6. To avoid scattered excitation light, the spectra were taken starting at 2 cm^{-1} below the excitation energy. The excitation laser was scanned over 2 GHz every 0.25 seconds to mitigate any holeburning effects. In the emission spectra of Fig. 6, vertical arrows are used to indicate the excitation energy. As the laser is tuned, ${}^3\text{H}_4(1a)$ and $(1b)$ levels from the various sites are excited. The ${}^3\text{H}_4(1b)$ excitation can emit directly to the ground state but it preferentially relaxes to the ${}^3\text{H}_4(1a)$ level before emission. The emission itself, which can be to the ${}^3\text{H}_6(1)$ or ${}^3\text{H}_6(2)$ levels, can be reabsorbed by other sites and go through this chain of events again. Thus the spectra can be quite complicated.

There are several features of note in the site-selective spectra:

1. The emission peaks have two basic widths. The broader ones have widths of $4\text{-}5 \text{ cm}^{-1}$; the narrower

ones have widths of $\sim 2 \text{ cm}^{-1}$, somewhat instrumentally broadened. The narrower lines are from the ${}^3\text{H}_4(1a) \rightarrow {}^3\text{H}_6(1)$ transitions and the broader ones are from the ${}^3\text{H}_4(1a) \rightarrow {}^3\text{H}_6(2)$ transitions.

2. A weak broad line was usually found $\sim 8 \text{ cm}^{-1}$ below the excitation energy. This is attributed to the ${}^3\text{H}_4(1a) \rightarrow {}^3\text{H}_6(2)$ emission when the ${}^3\text{H}_4(1a)$ level is directly excited by the laser.
3. A sharp line that corresponds to emission from the ${}^3\text{H}_4(1a) \rightarrow {}^3\text{H}_6(1)$ transition is generally present. This transition arises from exciting the ${}^3\text{H}_4(1b)$ level directly. The energy difference between the sharp line and the pump laser energy is an indication of the ${}^3\text{H}_4(1a) - {}^3\text{H}_4(1b)$ splitting for that site.
4. A broad line is always present $\sim 8 \text{ cm}^{-1}$ below any sharp emission line and corresponds to the ${}^3\text{H}_4(1a) \rightarrow {}^3\text{H}_6(2)$ transition.
5. The ${}^3\text{H}_4(1a) - {}^3\text{H}_4(1b)$ splittings are generally around 8 cm^{-1} . However, when pumping at 12607 cm^{-1} (top emission spectrum in Fig. 6), no sharp line was present. One explanation may be that a sharp line expected to occur around 15291.5 cm^{-1} could be reabsorbed due to the high absorption at that energy. Reabsorption also could be responsible for other broad peaks present in the selectively-excited spectra.
6. With multiple reabsorptions possible, the spectra presented in Fig. 5 should not be used for calculating the energy of ${}^3\text{H}_6(2)$. Rather, the earlier absorption experiment with temperature variation should be more reliable for obtaining that value. Because of reabsorption, the relative emission intensities shown in Fig. 5 are distorted and overstate the strength of transitions to ${}^3\text{H}_6(2)$ and other levels relative to the transition to ${}^3\text{H}_6(1)$.

We conclude that the first crystal field splitting of the ground multiplet is around 7.8 cm^{-1} . Since both ${}^3\text{H}_6(1)$ and ${}^3\text{H}_6(2)$ are singlets, this splitting presumably is less sensitive to the distortions from C_3 symmetry associated with charge compensation. The excited state ${}^3\text{H}_4(1)$ splittings, on the other hand, are more varied, ranging from 8 to 15 cm^{-1} ; in that case, it is reasonable to expect a greater variation from site to site due to the higher sensitivity of the doublet to perturbation.

With the insight thus gained and the following basic assumptions, we simulated the absorption line shape shown by the solid line in Figs. 3 and 6.

1. The total absorption arises from a combination of several sites.
2. Each site contributes a pair of absorption lines due to the lifting of the degeneracy associated with the E state ${}^3\text{H}_4(1)$, and both transitions from each pair have the same intensity and linewidth.

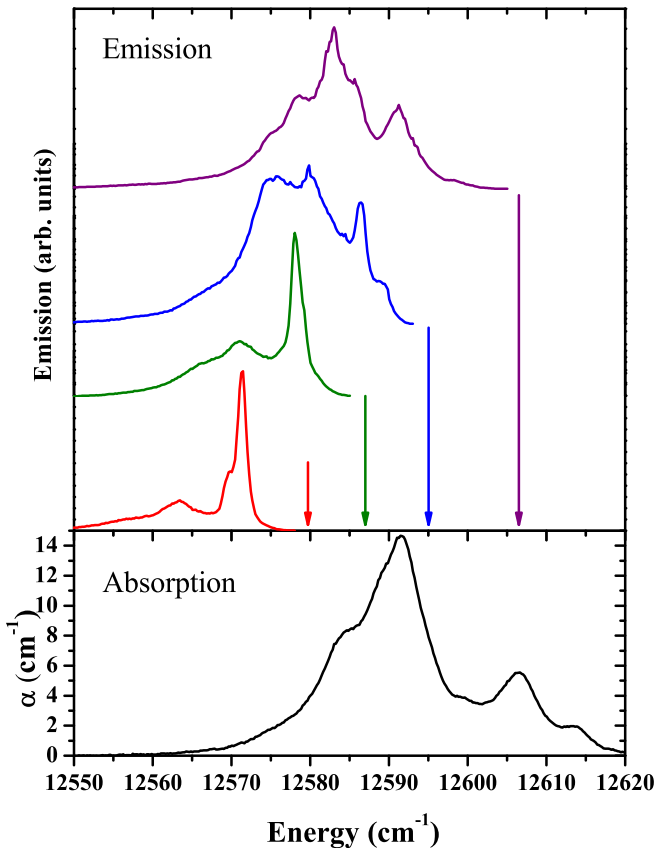


FIG. 6: σ polarized site-selective ${}^3\text{H}_4(1a)$ - ${}^3\text{H}_6(1$ and $2)$ emission spectra for 0.1% $\text{Tm}^{3+}:\text{LiNbO}_3$ at 1.6 K following cw laser excitation at positions indicated by the arrows.

3. Each absorption line has a Gaussian lineshape; Lorentzian tails are not compatible with the observations.
4. The values of the ${}^3\text{H}_4(1)$ splittings were clustered around 8 cm^{-1} and 15 cm^{-1} . These numbers were obvious from the emission spectrum presented in Fig. 6.

This simulation is shown in Fig. 7. Five sites were used, located at 12577.5 (9.5,10.0), 12584.6 (7.3,6.8), 12591.5 (15,6.0), 12592 (8,5.8), and 12599.2 (14.3,6.2) cm^{-1} , where the large values are the energies of the transitions to the lower component of each split doublet, the first number in each parenthesis is the energy splitting of that doublet and the second number corresponds to the FWHM linewidth. The two strongest components had similar intensity and were peaked at 12584.6 and 12591.5 cm^{-1} . All values for the transition energies were chosen by identifying specific features in the experimentally observed absorption lineshape. This simulation gives a satisfactory explanation of the measured absorption and explains a variety of other observations without the introduction of additional parameters. This interpretation of the level structure is further justified by the fact that the 1.7 K emission spectra do not give a spectral line above

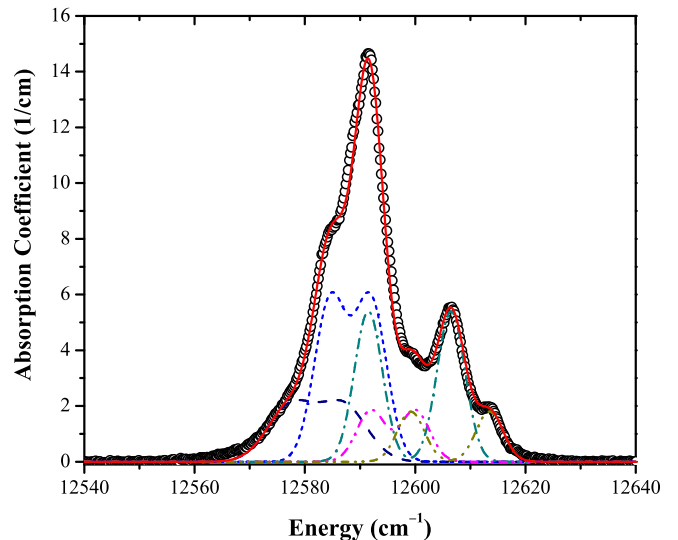


FIG. 7: Simulated absorption spectrum corresponding to five sites for the σ polarized ${}^3\text{H}_6(1)$ - ${}^3\text{H}_4(1a,1b)$ absorption spectrum for 0.1% $\text{Tm}^{3+}:\text{LiNbO}_3$. For each site, the lowest level in the excited ${}^3\text{H}_4$ multiplet is an E doublet that has been slightly split by reduction of the C_3 point symmetry by non-local charge compensation. Five sites were used in the simulation as stated in the text.

12600 cm^{-1} , because such transitions all would originate from the upper components of the ${}^3\text{H}_4(1)$ doublets. At the elevated temperature of 53 K, where the second components are thermally populated, emission corresponding to both components of the doublets was observed as expected.

The ${}^3\text{H}_6$ level structure may be deduced by combining the analysis of the polarized emission spectra with the absorption spectra observed for the lowest two levels of the ${}^3\text{H}_6$ multiplet. There are 5 singlet (A) levels and 4 doublet (E) levels expected. The energy levels are listed in Table III, along with the corresponding values determined in Ref. 26. Three transitions were very weak in the spectra. Although they are not easily seen when plotted on the scale given in Fig. 5, two were readily observable on a more sensitive scale. The only level with remaining uncertainty is from the transition at 12257 cm^{-1} . Contrary to the case of the ${}^3\text{H}_4$ multiplet, none of the ${}^3\text{H}_6$ assignments made by Ref. 20 were compatible with our observed spectra, but the partial list of energy levels that were presented in Ref. 26 agree with ours reasonably well. The energies that we list for higher levels were referenced to the main peak at 12591.5 cm^{-1} ; the very broad linewidth of that ${}^3\text{H}_6(1)$ - ${}^3\text{H}_4(1)$ transition can mean an uncertainty of up to 20 cm^{-1} . As discussed earlier, the relative intensities for the emission lines should be taken very cautiously because the measured values could be reduced by reabsorption.

Since we know the oscillator strengths from ${}^3\text{H}_6(1)$ to ${}^3\text{H}_4(1)$ and ${}^3\text{H}_6(2)$ to ${}^3\text{H}_4(1)$, we can calculate the contribution of these transitions to the spontaneous emission

TABLE III: Observed ${}^3\text{H}_4(1) \rightarrow {}^3\text{H}_6$ fluorescence transition energies and deduced ${}^3\text{H}_6$ levels. All transition linewidths are around 30 cm^{-1} . The intensity values are in arbitrary units.

E (cm^{-1})	Intens. (a.u.)	Polariz.	${}^3\text{H}_6$ (cm^{-1})	Irrep.	Ref. 26 (cm^{-1})
	114	σ	0	A	0
	154	σ	7.8	A	10
12504	weak	π, σ	79	E	
12436	72	σ	147	A	147
12360	weak	σ, π	223	E	
12314	42	π, σ	269	E	271
12257	weaker	π	326	E	
12225	32	σ	358	A	359
12147	10	σ	436	A	
					504

rate. The oscillator strengths for the ${}^3\text{H}_6(1)$ and ${}^3\text{H}_6(2)$ to ${}^3\text{H}_4(1)$ transitions were 2.0×10^{-6} and 2.7×10^{-6} , respectively. According to Di Bartolo,²¹ the radiative rate should be

$$\frac{1}{\tau_0} = \frac{1}{1.50} \frac{\text{cm}^2}{\text{s}} \cdot \frac{(n^2 + 2)^2}{9n} \frac{n^2}{\lambda_0^2} f_{21}. \quad (2)$$

With the known parameters, a contribution of $6.3 \times 10^3 \text{ s}^{-1}$ is obtained from these two transitions. That corresponds to a lifetime of $160 \mu\text{s}$. Due to contributions from transitions to other levels in the ${}^3\text{H}_6$ multiplet and to the ${}^3\text{F}_4$ and ${}^3\text{H}_5$ levels, we expect the actual rate to be somewhat faster, but the major contributions to the decay come from these two transitions. Transitions to other levels in the ${}^3\text{H}_6$ multiplet are much weaker and those to the ${}^3\text{F}_4$, and ${}^3\text{H}_5$ levels tend to contribute less to the decay rate because of the λ^{-2} dependence of the radiation rate.

Direct observation of the fluorescence lifetime, however, was not successful. When excited by an intense pulse, there was very little emission. We attribute the failure of observing T_1 directly to radiation trapping caused by the strong reabsorption present in this material and the relatively weak transition probability to the other levels of the ground multiplet as shown in Fig. 5. Stimulated emission may have also played a role in reducing fluorescence under those conditions and the relative intensities of the emission peaks to the higher levels in Fig. 5 could have been exaggerated. Figure 5 was obtained by much lower intensity CW excitation where reabsorption would only distort the relative strength of the peaks. The determination of T_1 is resolved in the following sections by both measuring three pulse echo decays and the observation of spectral hole decay; those experiments observe the transmission and coherent radiation and avoid radiation trapping and stimulated emission by directional, time, and wavelength selectivity.

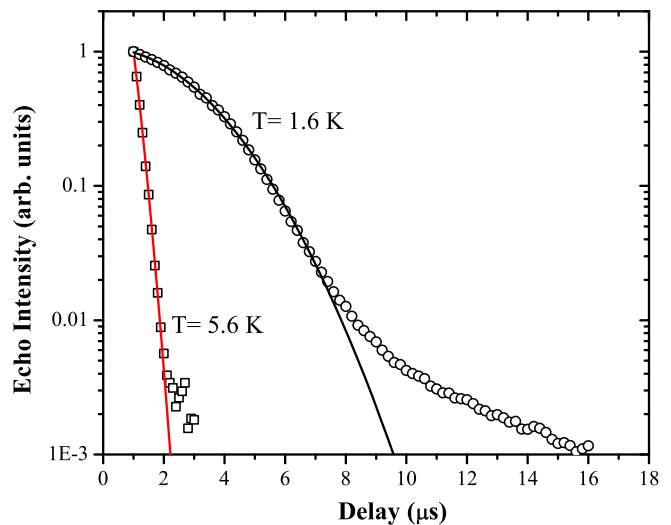


FIG. 8: Photon echo decay curves for 0.1%Tm:LiNbO₃ measured using two-pulse photon echoes at 5.6 K and 1.6 K are shown as data points. Fits to the experimental data are shown as lines. The 1.6 K data show a complex echo decay curve.

VI. OPTICAL DECOHERENCE: TWO-PULSE PHOTON ECHOES AND TEMPERATURE DEPENDENCE

To investigate the decoherence properties of the ${}^3\text{H}_6(1) \rightarrow {}^3\text{H}_4(1)$ transition and to characterize the mechanisms responsible for optical decoherence and the optical homogeneous linewidth, two-pulse photon echo decays were measured as a function of temperature over the range from 1.6 to 6.5 K. In addition, an echo excitation experiment determined the available signal processing bandwidth and provided further confirmation of the doublet splitting assignments made in Sec. III and V.

For photon echo experiments, excitation pulses of 100 ns were generated by modulating a single-frequency CW Ti:Sapphire laser with two acousto-optic modulators in tandem, as described earlier.²⁵ The experiments were carried out on a 0.91 mm thick sample with the light propagating along the a-axis and polarized along the a'-axis. The absorption is about 74% at the peak of 12591.5 cm^{-1} for that path length. We chose to investigate the decay behavior at a photon energy of 12578.4 cm^{-1} on the low energy side of the absorption where the absorption arises entirely from the ${}^3\text{H}_6(1) \rightarrow {}^3\text{H}_4(1a)$ transition. Sample decay curves are presented in Fig. 8. At the higher temperature (5.6 K), the decay is a simple exponential over the detectable range, as expected for more rapid decoherence due to phonon scattering. At lower temperatures, the echo decay is more complicated. The initial part of the decay curve has a shape that is quite characteristic for decays with spectral diffusion due to spin relaxation,²⁷ where time evolution of the spin dynamics causes the decay rate to change with time, reflecting a change in the homogeneous linewidth. The later part of

the decay, where the rate slows, is indicative of a time scale longer than that typical of spin flips, implying that some of the flipped spins have flipped again, returning to their original orientations. Such behavior was predicted by Hu and Walker.²⁸ Spin flips responsible for the spectral diffusion have a characteristic time of about 10 μ s at 1.6 K.

At lower temperatures, the influence of spectral diffusion makes it impossible to use a simple exponential decay with pulse delay time t_{12} for the echo intensities, and a fit to Mims' formula^{27,29} was used. The decay of the echo intensity I is then given by

$$I = I_0 e^{-2\left(\frac{t_{12}}{T_M}\right)^x} \quad (3)$$

where I_0 is the intensity of the echo at time $t_{12}=0$. The phase memory time T_M is very much dependent on the exponent x in the formula. We may determine the effective homogeneous linewidth over the timescale of the echo measurement using the relationship $1/\pi T_M$ as discussed in Ref. 30. The temperature dependence of the homogeneous linewidth Γ_h follows a model for direct phonon coupling as

$$\Gamma_h = \Gamma_0 + \frac{\Gamma_{ph}}{e^{\Delta E/k_B T} - 1} \quad (4)$$

where Γ_0 is the intrinsic linewidth of the transition, Γ_{ph} is the phonon coupling coefficient, ΔE is the energy of the level for the phonon to couple to, and k_B is Boltzmann constant. In the temperature range where $\Delta E \gg k_B T$, the contribution from phonons $\Gamma_h - \Gamma_0$ would approximate an exponential behavior relative to $1/T$. The temperature dependence of the decoherence is shown in Fig. 9, where the effective phonon contribution to the homogeneous linewidth is plotted versus temperature. By fitting to Eq. 4, we find that the temperature dependence is governed by coupling to a level at 7.2 cm^{-1} . This is very close to the 7.8 cm^{-1} energy of the ${}^3\text{H}_6(2)$ level in the ground state. Since the excited state energy gaps for the split doublets are not too different from the ground state gap, the temperature dependence of their contributions from phonon coupling could also be similar. The fitted phonon coupling coefficient of 1.11 MHz is quite small compared to the coupling coefficient of 34 MHz for 0.1%Tm:YAG.³¹ Also, Raman processes do not appear to contribute to the dephasing in this case.

While the linewidth is strongly temperature dependent over the range shown, Fig. 9 shows that sub-MHz linewidths are observed up to $T = 6.5$ K and above. The values at these higher temperature are still well within the acceptable limits for device applications.^{32,33}

To further explore the nature of the ${}^3\text{H}_6(1) \rightarrow {}^3\text{H}_4(1)$ transition and to determine how much of the absorption line was useful for SSH or quantum information applications, a photon echo excitation experiment was carried out at 1.6 K across the entire spectral region of the transition from 12566 to 12608 cm^{-1} . The excitation pulse

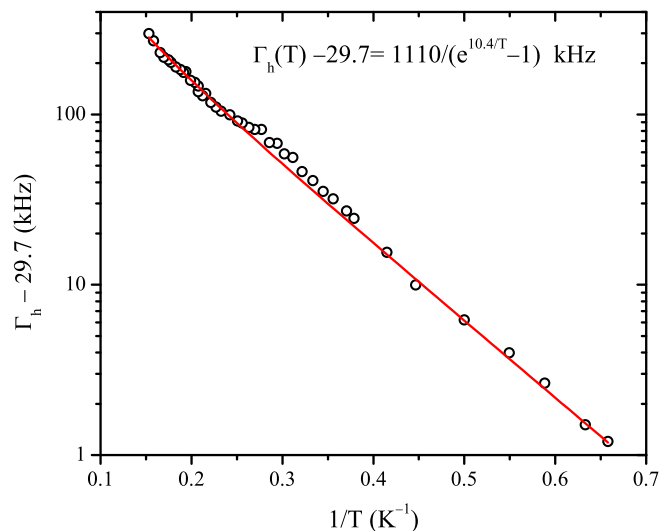


FIG. 9: Temperature dependence of the homogeneous linewidth Γ_h for 0.1%Tm:LiNbO₃ measured using two-pulse photon echoes as a function of temperature over the range from 1.6 to 6.5 K. The homogeneous linewidth is narrower than 0.5 MHz even at $T = 6$ K, indicating weak coupling to phonons for these levels in this material.

delays were fixed at 1 μ s, and the echo intensity was monitored while the laser frequency was changed. No effort was made, after the initial adjustment, to maximize the echo intensity by tuning other parameters or the sample alignment, only the photon energy was varied. Though there were strong variations in the absorption coefficients, instantaneous spectral diffusion was not expected to contribute significantly to the results at the laser intensities and pulse widths used in these measurements. The results are shown in the bottom graph of Fig. 10. In the top graph, we show the original absorption line and the absorption from the ${}^3\text{H}_6(1) \rightarrow {}^3\text{H}_4(1a)$ transition only (in dashed line), as expected from the analysis shown in Fig. 7, that will contribute to the echo generation. The echo excitation profile follows the absorption profile for the lower component ${}^3\text{H}_6(1a)$ quite nicely, and there is no echo observable above 12604 cm^{-1} . The absence of observable photon echoes at higher energy confirms our conclusion that the perturbed $\text{Tm}^{3+} {}^3\text{H}_4(1b)$ levels that correspond to the higher energy side of the absorption profile relax rapidly to those on the lower energy side.

Along with the echo intensity in the lower graph of Fig. 10, the expected echo intensity across the line is plotted. The expected intensity was calculated using Eq. A11 in the Appendix. Only the portion of the absorption associated with ${}^3\text{H}_6(1a)$ contributes to the generation of the photon echo signals and ${}^3\text{H}_6(1b)$ will not contribute to the echo as a consequence of the rapid population relaxation of this second component. The total absorption, however, still should be responsible for attenuation of the echo inside the crystal. Eq. A11 takes into consideration these factors and shows that the intensity is proportional

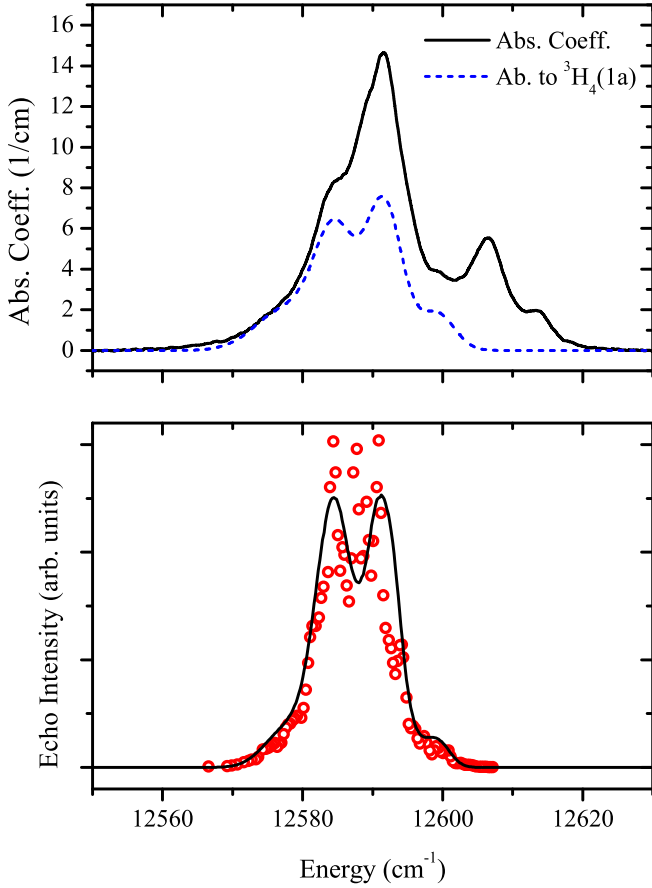


FIG. 10: Top: Measured absorption spectrum (solid line) and simulated spectrum for absorption due to ${}^3\text{H}_6(1) \rightarrow {}^3\text{H}_4(1a)$ only (dashed line). Bottom: Measured echo intensities (circles) and calculated echo intensities (line).

to $\beta^2 e^{-\alpha z}$ where β the absorption coefficient that produces echoes, α is the total absorption coefficient, and z is the optical path length where the focus is not tight enough to contribute to the echoes. The value of z is taken to be 0.5 mm in the plot in Fig. 10. Photon echoes were observable over a 30 cm^{-1} region, and the full-width at half-maximum region is about 12 cm^{-1} or 360 GHz. Since the absorption changes significantly across the profile, sometimes with rather high optical densities, the exact echo intensities should not be taken as a representation of the true decoherence behavior across the line. The photon echo intensities match the expected result, especially at the high and low end, adding further confirmation to the interpretation of the absorption profile as a sum of at least five split doublets and to the assertion that transitions to the lower components of the split doublets were mostly under the lower-energy portion of the absorption profile. We do not expect the middle and bottom graphs to match perfectly since Eq. A3 assumes small pulse areas only and the inferred absorption shown as the dashed line in the top graph also may not represent the ${}^3\text{H}_6(1a)$ absorption perfectly.

VII. OPTICAL DECOHERENCE: THREE-PULSE PHOTON ECHOES

The non-exponential decay at 1.6 K indicates the presence of spectral diffusion, which was investigated using three-pulse photon echoes. The separation between the first two echo excitation pulses t_{12} was kept constant, and the delay time t_{23} between the second and third excitation pulses was varied. For a nominal two-level system in a solid, the intensity decay of such a three-pulse echo, observed at time $2t_{12} + t_{23}$, can be described by²⁷

$$I(t_{12}, t_{23}) = I_0 e^{-2t_{23}/T_1} e^{-4t_{12}\pi\Gamma_{eff}(t_{12}, t_{23})} \quad (5)$$

For excitation to the ${}^3\text{H}_4$ level of Tm^{3+} , stimulated echoes are usually described using a three-level system. On account of population storage in the intermediate ${}^3\text{F}_4$ “bottleneck” level in Tm^{3+} crystals, the factor in Eq. 5 arising from spontaneous emission has to be changed to include the contributions of the bottleneck, such that

$$e^{-t_{23}/T_1} \rightarrow e^{-t_{23}/T_1} + \frac{\beta}{2} \frac{T_B}{T_B - T_1} (e^{-t_{23}/T_B} - e^{-t_{23}/T_1}) \quad (6)$$

where β is the branching ratio to the bottleneck level and T_B is the lifetime of the bottleneck level. The effective linewidth of the system can be expressed as

$$\Gamma_{eff}(t_{12}, t_{23}) = \Gamma_0 + \frac{1}{2} \Gamma_D [Rt_{12} + (1 - e^{-Rt_{23}})] \quad (7)$$

where Γ_D represents the spectral diffusion due to magnetic dipole fluctuations in the environment. The factor R describes the rate of dipole fluctuations. Such spectral diffusion has been observed in many other systems, including $\text{Er}:\text{Y}_2\text{SiO}_5$ where electron spins fluctuate²⁷ and $\text{Eu}:\text{YAlO}_3$, where nuclear spins fluctuate.³⁴

Three-pulse echo decays in the present work were measured at 1.7 K with $t_{12} = 0.5 \mu\text{s}$ and with t_{23} varied up to 15 ms. Separate scans were made using several time ranges so that time scales ranging over more than three decades were well represented in the experimental data. The different scans were then combined into one data set and fitted to Eq. 5 with the substitutions expressed in Eq. 6 and Eq. 7. The data and the fit are presented in Fig. 11. In the initial analysis, the fluorescence lifetime T_1 was treated as an unknown parameter, since it was not measured directly by optical emission as a result of the large oscillator strength and consequent reabsorption for the ${}^3\text{H}_6(1) \rightarrow {}^3\text{H}_4(1)$ transition in this material. Fitting to the data showed that T_1 is $152 \mu\text{s}$ and the branching ratio is 0.27 with a bottleneck lifetime of 7 ms. We note here that these last two parameters were correlated. With the limited range of data, there could be large uncertainties in those two values; however, the bottleneck lifetime thus obtained is consistent with measured ${}^3\text{F}_4$ T_1 values for other Tm^{3+} doped materials. For spectral diffusion at 1.6 K, the fit shows that the homogeneous linewidth is 30 kHz at short times (which is also measured by two pulse echoes) and that it has a maximum

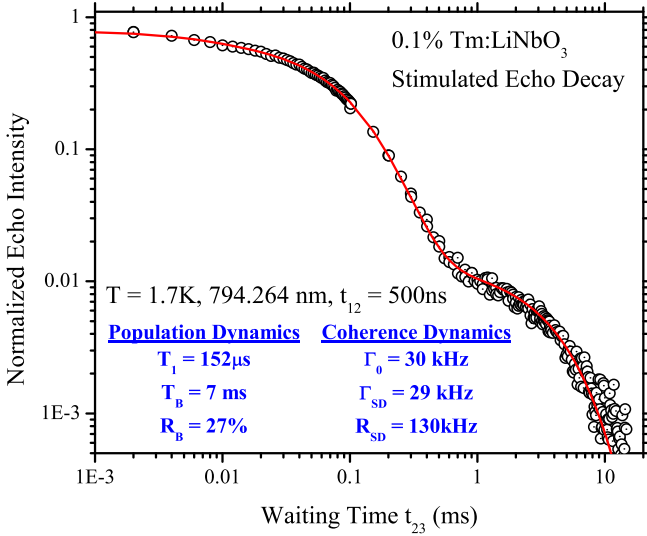


FIG. 11: Stimulated echo decay curve for 0.1%Tm:LiNbO₃ at 1.6 K. The solid curve drawn through the data is a fit of Eqs. 5, 6, and 7 using the material parameters given in the figure.

broadening of 29 kHz due to spin flips occurring at a 130 kHz rate. This rate is consistent with the data shown in Fig. 8 where the decay curve bends over at around 10 μ s, which corresponds to a similar frequency. The spins causing this spectral diffusion are expected to be the Tm³⁺ “enhanced nuclear moments” arising from the small energy gaps in both the ground and excited states.^{35,36} We also note that direct spectral hole burning measurements provided an alternate experimental technique for determining T_1 , and those measurements indicated the bottleneck lifetime to be 4.5 ms and the excited state lifetime to be 160 μ s.²⁵

VIII. DECAY OF A SPECTRAL HOLE AND EXCITED STATE POPULATION DECAY DYNAMICS

Other important aspects of the material physics that must be understood for use of Tm:LiNbO₃ in applications are the relaxation rates and pathways for the Tm³⁺ excited ³H₄ state. To explore these processes, we employed both time-resolved spectral hole burning techniques as well as stimulated photon echo spectroscopy. Earlier efforts to monitor fluorescence decay from the ³H₄ state were unsuccessful, perhaps due to radiation trapping effects, so that traditional approach was not pursued in this work.

The experimental arrangement used for spectral hole burning measurements was similar to the approach used to measure photon echoes (see Section VI), except that a Toptica external cavity diode laser (ECDL) in the Littrow configuration was used. Linear frequency chirps were applied to one of the laser pulses and the laser trans-

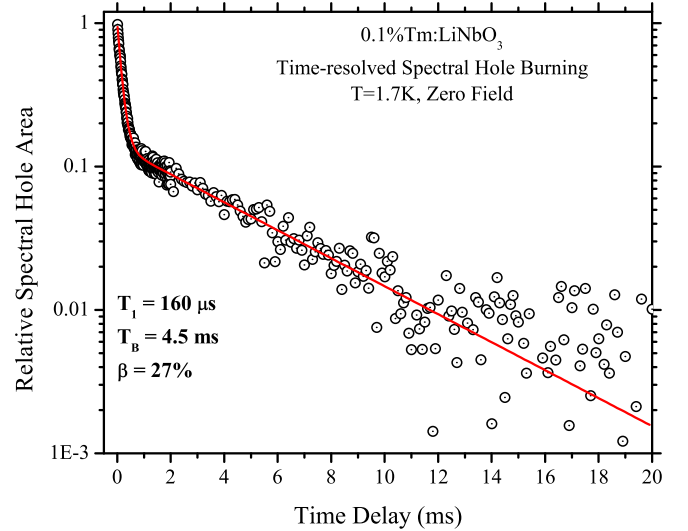


FIG. 12: Measured transient spectral hole decay. The fit of the theoretical model allows us to extract the excited-state lifetime and the relaxation branching ratios.

mission was directly monitored. Frequency chirps were generated by either modulating the laser diode current for rapid scans over a few hundred MHz, or by scanning a piezo-electric transducer to scan over larger ranges of GHz. Typical chirp rates were several MHz/ms and an SRS DS-345 signal generator produced the synchronized driving signals. The output of the laser was sent through a variable attenuator to allow the intensity at the sample to be controlled. Transmission through a Fabry-Perot with a free spectral range of 99.16 MHz was simultaneously monitored to calibrate the laser frequency chirp. Two pulses were applied to the sample, with the first high-intensity pulse at a fixed frequency to saturate the population and burn a spectral hole. The second pulse was attenuated by several orders of magnitude and synchronized with the laser frequency chirp to read out the spectral hole transmission spectrum generated by the first burn pulse. The widths of the spectral holes were typically several MHz, limited by the frequency stability of the laser. The repetition rate was chosen to be long enough that all of the excited ions relaxed between each measurement.

Time-resolved spectral hole burning measurements of the population relaxation were carried out by recording the change in integrated absorption coefficient due to the spectral hole. Since the integrated absorption coefficient is proportional to the population difference between the ³H₆ and ³H₄ levels, the population dynamics can be directly extracted from the spectral hole decays. Furthermore, by scanning over the entire spectral hole shape, detrimental effects of laser frequency jitter or spectral diffusion broadening were eliminated. An example of a measured spectral hole decay is plotted in Figure 12.

By analyzing the decay of the spectral hole areas shown in Figure 12, we may determine the ³H₄ lifetime, the re-

laxation pathways, and the 3F_4 bottleneck lifetime. The hole lifetime follows a similar decay as described in Eq. 6 and the bottleneck lifetime was determined to be 4.5 ms with an initial decay of 160 μ s which is consistent with earlier determination using three pulse echoes. The bottleneck lifetime has a larger error due to the limited range in time available in the data.

IX. SUMMARY AND DISCUSSION

We have elucidated the energy level structure of $\text{Tm}^{3+}:\text{LiNbO}_3$ for both the 3H_6 and 3H_4 multiplets. We assigned both the ground state ${}^3H_6(1)$ and ${}^3H_6(2)$ levels as singlets, and the lowest excited state levels ${}^3H_4(1a,1b)$ as a split E doublet, with the splitting arising from the deviation from C_3 symmetry as a consequence of charge compensation. That assignment came from analysis of the polarization behavior of the transitions and their line-shapes. Simulations assuming five sites with the same transition probability for each component of a doublet describe the absorption profile well. The splitting of doublets is expected to be more sensitive to deviations from C_3 symmetry than the splitting of a pair of singlet levels already split in C_3 symmetry, and this was the case. The energy gaps between ${}^3H_6(1)$ and ${}^3H_6(2)$ are nominally 7.8 cm^{-1} for all sites, but the splittings for ${}^3H_4(1a,1b)$ spanned from 7.3 to 15 cm^{-1} . The singlet assignment of the ground state was consistent with that of Ref. 20 and with all of our observations. Our analysis of the 3H_6 levels, however, differed from Ref. 20. For 3H_4 , our assignments were similar to Ref. 20. Combining the new results from this work and those from Ref. 20, a crystal field fit should be possible using the underlying C_3 symmetry, and it is reasonable to expect that the resulting wavefunctions could yield better understanding of the states and splittings associated with the lowered symmetry.

Interestingly, almost all of the optical transition strength is concentrated between the lowest levels of the 3H_6 ground-state multiplet and the 3H_4 excited-state multiplet, an ideal situation.

For the ${}^3H_6(1)\rightarrow{}^3H_4(1)$ transition, the absorption strength is 250 cm^{-2} . The remaining transitions, from ${}^3H_6(1)\rightarrow{}^3H_4(2)$ to ${}^3H_6(1)\rightarrow{}^3H_4(6)$, add up to 47 cm^{-2} for the σ transitions and 50 cm^{-2} for the π transitions. Considering the weights for polarizations, the ${}^3H_6(1)\rightarrow{}^3H_4(1)$ transition accounts for 78% of the total transition strength of the ${}^3H_6(1)\rightarrow{}^3H_4$ transitions. Similarly, all of the emissions were mostly into the two lowest levels in the ground state. The ${}^3H_6\rightarrow{}^3H_4$ transition in $\text{Tm}^{3+}:\text{LiNbO}_3$ has a much larger oscillator strength compared to that in $\text{Tm}^{3+}:\text{YAG}$ which has been the standard material in Tm^{3+} coherence spectroscopy and applications. With nominal 0.1 at. % doping, the absorption coefficient is $\sim 1.7\text{ cm}^{-1}$ for $\text{Tm}^{3+}:\text{YAG}$ and $\sim 15\text{ cm}^{-1}$ for $\text{Tm}^{3+}:\text{LiNbO}_3$, while the integrated intensity of each is 1.6 cm^{-2} and 125 cm^{-2} (for ${}^3H_4(1a)$ only), respec-

tively. Considering the ion densities, indices of refraction, and other material parameters, the absorption oscillator strength of $\text{Tm}^{3+}:\text{LiNbO}_3$ is 2.0×10^{-6} , 25 times that of $\text{Tm}^{3+}:\text{YAG}$. The $\text{Tm}^{3+}:\text{LiNbO}_3$ transition will have a Rabi frequency 5 times larger for the same optical excitation. We should also point out that in YAG, the cubic crystal symmetry leads to multiple site orientations so that a single optical polarization only excites a subset of all the ions (at most one third).²³ In contrast, if we assume an ideal C_3 axial symmetry for Tm^{3+} in LiNbO_3 , all of the Tm^{3+} ions may be fully excited using a single circular polarization. However, our measurements indicate that the C_3 symmetry is slightly distorted and the doublet is split. As a result, further detailed studies of these sites are required to determine the effect of the distortion on the polarization dependence.

The homogeneous linewidth was measured to be 30 kHz at 1.6 K and to be ~ 350 kHz at 6.5 K. The energy level structure allowed us to understand the temperature-dependent behavior of the homogeneous linewidth as determined by direct processes associated with the ${}^3H_6(2)$ in the ground state and ${}^3H_4(1b)$ level in the excited state. Though the ${}^3H_4(1a,b)$ energy gaps range from 7.3 to 15 cm^{-1} , we do not expect the temperature dependence of the homogeneous linewidth to vary significantly among the charge-compensated sites because the ground state energy gap does not vary significantly for the different sites. The phonon coupling coefficient is small in this material, on the order of 1.1 MHz, in contrast to the 34 MHz coupling coefficient for 0.1% $\text{Tm}:\text{YAG}$.

Photon echo excitation measurements carried out across the entire absorption line indicated that the echo intensity was determined by the absorption due to the ${}^3H_4(1a)$ level for each site and by attenuation from the total absorption. The width of the echo excitation curve was approximately 12 cm^{-1} or 360 GHz, in strong contrast with the $<1\text{ cm}^{-1}$ of $\text{Tm}:\text{YAG}$. With the 30 kHz homogeneous linewidth at 1.6 K, and the useful width of 12 cm^{-1} in the absorption line, we have a ratio of the inhomogeneous to homogeneous linewidth, which sets an upper limit on the time-bandwidth product for signal processing, as high as 1.2×10^7 . This dramatically increased time-bandwidth product could be exploited due to the much faster Rabi frequency in $\text{Tm}^{3+}:\text{LiNbO}_3$ associated with the 25 times increase in transition oscillator strength. Three pulse echo measurements indicated that the spectral diffusion is dominated by magnetic interactions arising from the large enhanced nuclear moment of Tm^{3+} , which is due to the small energy gaps in both the ground and excited states. Interactions between $\text{Tm}^{3+}\text{-Li}$ and $\text{Tm}^{3+}\text{-Nb}$ could also contribute to the spectral diffusion. It should be possible to slow down the spectral diffusion by applying an external magnetic field. Measurements by Thiel et. al. in a magnetic field have confirmed that sensitivity.²⁵ The three pulse echo measurements also established a lower limit on the spontaneous emission lifetime T_1 for ${}^3H_4(1a)$ of 152 μ s. We also note that this is essentially the spontaneous emission lifetime

limit calculated from the transition probabilities. The bottleneck lifetime in the 3F_4 level was estimated at 7 ms, similar to values in other systems including $\text{Tm}^{3+}:\text{YAG}$. The branching ratio was estimated to be 0.27, slightly smaller than for $\text{Tm}^{3+}:\text{YAG}$ where it is 0.5, likely due in part to the large transition probability for relaxation to 3H_6 in LiNbO_3 .

We point out that an upper state lifetime of 226 μs was reported for $0.06\%\text{Tm}^{3+}:\text{LiNbO}_3$.³⁷ This value is longer than what our oscillator strength measurement indicates is possible. However, emission lifetime measurement is always difficult for large oscillator strength samples because of reabsorption. For the bottleneck lifetime, we observe 7 ms in the stimulated echoes and 4.5 ms in the holeburning decay. In the literature, this lifetime was reported to be 2.45 ms by a direct measurement of the 1.7 μm transition in bulk crystals³⁷ and waveguides.^{38,39} The differences are quite significant and need further explanation, especially considering that this lifetime is essentially concentration independent.³⁷ We think the different measurements may be sampling different groups of ions in the material, resulting in the the different values of the bottleneck lifetime. In a direct emission measurement, the total ensemble of the Tm ions are sampled. In a stimulated echo measurement, only those ions with long coherence time are sampled. Those ions tend to be better isolated compared to the general Tm population and thus experience less cross relaxation with other ions that can reduce the lifetime. In holeburning experiments, we have an intermediate situation where we are still preferentially choosing part of the absorption line that tends to have longer coherence times but we are using a non-coherent technique. The range of material compositions for ‘‘congruent’’ LiNbO_3 may be also a factor.

Appendix A: Dependence of the echo intensity on absorption

Most textbooks give the echo intensity as a function of the absorption strength and the pulse areas used in echo generation.⁴⁰ However, in our simulations for Fig. 8(c) in sec. VI, the absorption does not contribute uniformly to echo generation. For example, at the maximum absorption around 12591 cm^{-1} , about half of the absorption is due to the transition to ${}^3H_4(1b)$ and thus will not produce echoes and only absorbs the echo and the excitation pulses. Consequently, we must derive the echo intensity when such non-productive absorption is present. In the following discussion, α is the total absorption coefficient and β is the part of the absorption coefficient that is associated with echo generation. We start with the standard echo equations of Allen and Eberly.⁴⁰ In the normal case when all absorption produces echoes, for small pulse areas the three main equations are:

$$\frac{d\theta_1}{dt} \approx -\frac{\alpha}{2}\theta_1(z)$$

$$\begin{aligned} \frac{d\theta_2}{dt} &\approx -\frac{\alpha}{2}\theta_2(z) \\ \frac{d\theta_e}{dt} &\approx \frac{\alpha}{4}\theta_1(z)[\theta_2(z)]^2 - \frac{\alpha}{2}\theta_e(z) \end{aligned} \quad (\text{A1})$$

where θ_1 and θ_2 are areas of the excitation pulses, θ_e is the area of the echo, and z is the distance along the propagation direction.

However, when only a portion of the the absorption is responsible for the echoes, as in our case, these equations must be modified such that

$$\begin{aligned} \frac{d\theta_1}{dt} &= -\frac{\alpha}{2}\theta_1(z) \\ \frac{d\theta_2}{dt} &= -\frac{\alpha}{2}\theta_2(z) \\ \frac{d\theta_e}{dt} &= \frac{\beta}{4}\theta_1(z)[\theta_2(z)]^2 - \frac{\alpha}{2}\theta_e(z) \end{aligned} \quad (\text{A2})$$

where β is the absorption coefficient responsible for the generation of echoes.

Solving the first two equations and substituting into the third, we get an equation similar to Eq.(9.30) in Ref. 40

$$\frac{d\theta_e}{dt} = -\frac{\alpha}{2}\theta_e(z) + \frac{\beta}{4}\theta_1(0)\theta_2^2(0)e^{-\frac{3}{2}\alpha z} \quad (\text{A3})$$

For solution of this equation, we assume a form of

$$\theta_e = Ae^{-\gamma z} + Be^{-\delta z} \quad (\text{A4})$$

Substituting Eq. A4 into Eq. A3, we get

$$-\gamma Ae^{-\gamma z} - \delta Be^{-\delta z} = -\frac{\alpha}{2}Ae^{-\gamma z} - \frac{\alpha}{2}Be^{-\delta z} + \frac{\beta}{4}\theta_1(0)\theta_2^2(0)e^{-\frac{3}{2}\alpha z} \quad (\text{A5})$$

To satisfy this equation, we can make either γ or δ to be $3\alpha/2$ and get the same final result. If we choose $\gamma=3\alpha/2$, we have

$$\begin{aligned} \gamma &= \frac{3\alpha}{2} \\ -\gamma A &= -\frac{\alpha}{2}A + \frac{\beta}{4}\theta_1(0)\theta_2^2(0) \\ -\delta B &= -\frac{\alpha}{2}B \end{aligned} \quad (\text{A6})$$

which leads to

$$\begin{aligned} \gamma &= \frac{3\alpha}{2} \\ \delta &= \frac{\alpha}{2} \\ A &= -\frac{\beta}{4\alpha}\theta_1(0)\theta_2^2(0) \end{aligned} \quad (\text{A7})$$

The solution is

$$\theta_e = -\frac{\beta}{4\alpha}\theta_1(0)\theta_2^2(0)e^{-\frac{3}{2}\alpha z} + Be^{-\frac{1}{2}\alpha z} \quad (\text{A8})$$

Since the echo should have zero intensity at $z=0$, we thus have

$$\theta_e = \frac{\beta}{2\alpha} \theta_1(0) \theta_2^2(0) e^{-\alpha z} \sinh \frac{\alpha z}{2} \quad (\text{A9})$$

In other words, the echo is only reduced by a factor of $(\beta/\alpha)^2$, since the echo intensity is proportional to θ_e^2 .

In an optical experiment, the optical beam is generally not collimated but rather focussed into the sample. Only in a small portion of the optical path is the pulse area large enough for significant generation of echoes. Frequently, this portion is in the front part of the sample. Assuming that this section (length z') is short enough so that $\alpha z'$ is small, then the above equation simplifies to

$$\theta_e \approx \frac{\beta z'}{4} \theta_1(0) \theta_2^2(0) \quad (\text{A10})$$

If the extra length in the optical path is z then the signal strength s is

$$s \propto \beta^2 e^{-\alpha z} \quad (\text{A11})$$

This is the simplification that we use for our simulation in Fig. 10.

Acknowledgments

The authors would like to thank R. M. Macfarlane for many fruitful discussions. Research at the Department of Physics, Montana State University was supported in part by the US Air Force Research Laboratory under Agreement Nos. F49620-97-1-0411, F49620-98-1-0171, F49620-01-1-0313, and F49620-00-1-0314; the Army Research Office under contract no. W911NF-05-1-0358; and the National Science Foundation under grant no. 0903937. Any opinions, findings, and conclusions or recommendations expressed in this material are those of the authors and do not necessarily reflect the views of the the Air Force Research Laboratory, Army Research Office, or National Science Foundation.

- * Electronic address: yxsun@usd.edu
- † Electronic address: thiel@physics.montana.edu
- ‡ Electronic address: cone@montana.edu
- ¹ R. K. Mohan, T. Chang, M. Tian, S. Bekker, A. Olson, C. Ostrander, A. Khallaayoun, C. Dollinger, W. R. Babbitt, Z. Cole, et al., *Journal of Luminescence* **127**, 116 (2007).
 - ² W. R. Babbitt and J. A. Bell, *Applied Optics* **33**, 1538 (1994).
 - ³ K. D. Merkel, R. K. Mohan, Z. Cole, T. Chang, A. Olson, and W. R. Babbitt, *Journal of Luminescence* **107**, 62 (2004).
 - ⁴ K. D. Merkel, W. R. Babbitt, K. E. Anderson, and K. H. Wagner, *Optics Letters* **24**, 1386 (1999).
 - ⁵ W. Tittel, M. Afzelius, T. Chaneliere, R. L. Cone, S. Kroll, S. A. Moiseev, and M. Sellars, *Laser & Photonics Reviews* **4**, 244 (2010).
 - ⁶ M. Tian, Z. W. Barber, J. A. Fischer, and W. R. Babbitt, *Phys. Rev. A* **69**, 050301 (2004), URL <http://link.aps.org/doi/10.1103/PhysRevA.69.050301>.
 - ⁷ O. Guillot-Noël, P. Goldner, E. Antic-Fidancev, and J. L. Le Gouët, *Phys. Rev. B* **71**, 174409 (2005), URL <http://link.aps.org/doi/10.1103/PhysRevB.71.174409>.
 - ⁸ A. Louchet, J. S. Habib, V. Crozatier, I. Lorgeré, F. Goldfarb, F. Bretenaker, J.-L. Le Gouët, O. Guillot-Noël, and P. Goldner, *Phys. Rev. B* **75**, 035131 (2007), URL <http://link.aps.org/doi/10.1103/PhysRevB.75.035131>.
 - ⁹ F. de Seze, A. Louchet, V. Crozatier, I. Lorgeré, F. Bretenaker, J.-L. Le Gouët, O. Guillot-Noël, and P. Goldner, *Phys. Rev. B* **73**, 085112 (2006), URL <http://link.aps.org/doi/10.1103/PhysRevB.73.085112>.
 - ¹⁰ E. Saglamyurek, N. Sinclair, J. Jin, J. A. Slater, D. Oblak, F. Bussières, M. George, R. Ricken, W. Sohler, and W. Tittel, *Nature* **469**, 512 (2011).
 - ¹¹ R. Weis and T. Gaylord, *Appl. Phys. A* **37**, 191 (1985).
 - ¹² V. Dierolf and M. Koerdt, *Phys. Rev. B* **61**, 8043 (2000).
 - ¹³ G. Malovichko, V. Grachev, A. Hofstaetter, E. Kokanyan, A. Scharmann, and O. Schirmer, *Phys. Rev. B* **65**, 224116 (2002).
 - ¹⁴ R. M. Macfarlane, F. Könz, Y. Sun, and R. L. Cone, *J. Lumin.* **86**, 311 (2000).
 - ¹⁵ D. M. B. P. Milori, I. J. Moraes, A. C. Hernandez, R. R. de Souza, M. S. Li, M. C. Terrile, and G. E. Barberis, *Phys. Rev. B* **51**, 3206 (1995).
 - ¹⁶ D. M. Gill, L. McCaughan, and J. C. Wright, *Phys. Rev. B* **53**, 2334 (1996), URL <http://link.aps.org/doi/10.1103/PhysRevB.53.2334>.
 - ¹⁷ J. García Solé, L. Bausá, D. Jaque, E. Montoya, H. Murrrieta, and F. Jaque, *Spectrochimica Acta Part A* **54**, 1571 (1998).
 - ¹⁸ T. Nolte, T. Pawlik, and J. M. Spaeth, *Solid State Communications* **104**, 535 (1997).
 - ¹⁹ A. Lorenzo, H. Jaffrezic, B. Roux, G. Boulon, and J. García-Solé, *Applied Physics Letters* **67**, 3735 (1995).
 - ²⁰ L. Núñez and F. Cussó, *J. Phys.: Condens. Matter* **5**, 5301 (1993).
 - ²¹ B. D. Bartolo, *Optical Interactions in Solids* (John Wiley & Sons, Inc, New York, 1968).
 - ²² B. Henderson and G. F. Imbush, *Optical Spectroscopy of Inorganic Solids* (Oxford Science Publications, Clarendon Press, Oxford, 2006).
 - ²³ Y. Sun, G. M. Wang, R. L. Cone, R. W. Equall, and M. J. M. Leask, *Phys. Rev. B* **62**, 15443 (2000).
 - ²⁴ R. M. Macfarlane and R. M. Shelby, *Spectroscopy of Solids Containing Rare Earth Ions* (North Holland, 1987), chap. 3.
 - ²⁵ C. W. Thiel, Y. Sun, T. Böttger, W. R. Babbitt, and R. L. Cone, *J. of Lumin.* **130**, 1598 (2010).
 - ²⁶ L. F. Johnson and A. A. Ballman, *J. Appl. Phys.* **40**, 297 (1969).
 - ²⁷ T. Böttger, C. W. Thiel, Y. Sun, and R. L. Cone, *Physical Review B* **73**, 075101 (2006).
 - ²⁸ P. Hu and L. R. Walker, *Phys. Rev. B* **18**, 1300 (1978).
 - ²⁹ W. B. Mims, *Phys. Rev.* **168**, 370 (1968), URL <http://link.aps.org/doi/10.1103/PhysRev.168.370>.
 - ³⁰ C. W. Thiel, R. M. Macfarlane, T. Böttger, Y. Sun, R. L. Cone, and W. R. Babbitt, *Journal of Luminescence* **130**, 1603 (2010).
 - ³¹ Y. Sun and R. L. Cone, Private Communications.
 - ³² Y. Sun, *Spectroscopic Properties of Rare Earths in Optical Materials* (Springer-Verlag, 2005), chap. 7, pp. 379–429.
 - ³³ C. W. Thiel, T. Böttger, and R. L. Cone, *J. of Lumin.* **131**, 353 (2011).
 - ³⁴ R. Yano, M. Mitsunaga, and N. Uesugi, *Phys. Rev. B* **45**, 12752 (1992), URL <http://link.aps.org/doi/10.1103/PhysRevB.45.12752>.
 - ³⁵ B. Bleaney, *Physica* **69**, 317 (1973).
 - ³⁶ A. Abragam and B. Bleaney, *Proc. Roy. Soc. (Lond.)* **A387**, 221 (1983).
 - ³⁷ M. Quintanilla, E. Cantelar, J. Sanz-García, G. Lifante, G. Torchia, and F. Cussó, *Journal of Luminescence* **128**, 927 (2008), ISSN 0022-2313.
 - ³⁸ N. Sinclair, E. Saglamyurek, M. George, R. Ricken, C. L. Mela, W. Sohler, and W. Tittel, *Journal of Luminescence* **130**, 1586 (2010), ISSN 0022-2313.
 - ³⁹ E. Cantelar, G. A. Torchia, J. Sanz-García, P. L. Pernas, G. Lifante, and F. Cussó, *Physica Scripta* **T118**, 69 (2005).
 - ⁴⁰ L. Allen and H. J. Eberly, *Optical Resonance and Two-Level Atoms* (Dover, 1987).